

Contrail formation in aircraft wakes

By **Roberto Paoli** [†], **Jerome Hélie** & **Thierry Poinso** [‡]

(Received 25 November 2003)

The process of formation and early evolution of a condensation trail ("contrail") in the near-field of an aircraft wake was numerically studied by means of a mixed Eulerian/Lagrangian two-phase flow approach. Large-eddy simulations were used for the carrier phase, while, for the dispersed phase, a Lagrangian particle tracking method was used, coupled to a microphysics model to account for ice nucleation. The basic configuration was an exhaust engine jet loaded with soot particles and water vapor and interacting with a wing-tip trailing vortex. The thermodynamic conditions for contrail formation were identified by tracking the spatial distribution of supersaturation around particles. A strong mass coupling between the two phases was demonstrated by the simulations: the condensation of water vapor over soot particles, induced by exhaust dispersion into cold ambient air, leads to the formation of ice crystals whose sizes grow until thermodynamic equilibrium between the two phases is reached. Finally, local vapor depletion causes significant deviation from the classical mixing line theory and is also responsible for polydispersion of particles radii.

1. Introduction

Contrails are ice clouds generated by water exhaust gases from aircraft reactors, forming the common visible white lines in the sky. As assessed in the special report of the Intergovernmental Panel on Climate Change (IPCC report (1999)), they have an important environmental impact because they artificially increase cloudiness and trigger the formation of cirrus clouds, thus altering climate both on local and regional/global scales. This was confirmed in a recent climate study (Travis & *al.* (2002)) performed in the three days following the 11th of September 2001, when all american civilian aircrafts were grounded and no contrails existed over the USA. During this period, abnormal and significant temperature differences between day and night (namely, "daily temperature range" or DTR) were observed in the USA.

Contrails consist of ice crystals which mainly form by condensation of exhaust water vapor over suitable nucleation sites, like soot particles and sulfur aerosols, emitted by aircraft engines (Schumann (1996), Karcher & *al.* (1996)). The microphysics of ice formation has been widely investigated during the last years (see Pruppacher & Klett (1997) for a complete review) and was found to be strongly affected by atmospheric conditions as well as engine parameters like the type of fuel. In particular, for low fuel sulfur content and low ambient temperature, direct heterogeneous freezing of ice on soot particles compete with the sulfur enhanced activation path into water droplets. In such a case, contrails form when the air surrounding the particles becomes supersaturated with respect to ice (Schumann (1996)). For certain atmospheric conditions, this may occur somewhere in the jet plume, as the result of the increased humidity due to mixing between hot and moist exhaust gases with cold and less humid ambient air. In a vapor pressure-temperature plane (see Fig. 1), assuming that vapor and heat diffuse at the same speed and that the flow is adiabatic, pure mixing can be graphically represented by a straight ("mixing") line which

[†] CERFACS, 42 Avenue Gaspard Coriolis, 31057 Toulouse, France

[‡] IMFT, Allée du Professeur Camille Soula, 31400 Toulouse, France

is completely defined by the two states A (ambient air) and B (exhaust gas). In Fig. 1, supersaturation corresponds to the thermodynamic states laying between S_1 and S_2 , where $p_w > p_{sat}(T)$. An ice crystal forms when such a condition is locally satisfied in the jet plume and, at the same time, a nucleation particle is present. Background atmospheric vapor, which eventually adds to the exhaust content, is responsible for the persistence of contrails (Gierens (1996)). Formation and persistence of contrails have been studied during the last years, mostly in atmospheric science literature, through *in situ* measurements and numerical simulations with different levels of complexity (see IPCC report (1999) and references therein). Using sophisticated microphysics and radiative models (generally employing "bulk" formulation for the ice phase) those authors analyzed the development (e.g. Sussmann & Gierens (1999)) and persistence (e.g. Gierens (1996)) of contrails and their interaction with atmosphere on time scales of the order of minutes and tens of minutes from the emission time.

The present work focuses on the simulation of contrail formation and early evolution in the near-field of an aircraft wake, i.e. up to a few seconds from the emission time. To that end a two-phase flow approach is used, by assuming that the medium consists of a gaseous carrier phase and a solid, dispersed phase (ice crystals). Large-eddy simulations have been used for the carrier phase, as they were found to be well suited to deal with inherently unsteady phenomena taking place at flight Reynolds number, such as jet and wake vortex instabilities (Le Diz  s & Laporte (2002), Paoli & al. (2003)). A Lagrangian particles tracking method has been used for the dispersed phase to track particles motion. The basic configuration consists of an exhaust jet, loaded with water vapor and soot particles, interacting with a wing-tip trailing vortex (see Paoli & al. (2003) for a discussion of jet/vortex interaction in the near-field of the wake). The objective of the simulations is two-fold: first, provide a detailed 3D description of the condition for ice formation in the exhaust jet and the effects of the wake vortex, by analyzing the spatial distribution of supersaturation around particles. Then, the formation and early evolution of the contrail and its influence on vapor mixing with ambient air are analyzed, by exploiting a simple microphysics model for ice growth, derived from atmospheric science literature (Karcher & al. (1996)). The governing equations for the two-phase flow model and the results of the simulations are presented, respectively, in Sec. 2 and Sec. 3, conclusions on the main outcomes of this study are finally given in Sec. 4.

2. Governing equations and ice microphysics model

Large-eddy simulations of ice formation are carried out through an Eulerian/Lagrangian two-phase flow approach. For the gaseous (carrier) phase the fully compressible Navier-Stokes equations are solved together with a transport equation for a scalar field Y_w , representing the exhaust water vapor. These equations are filtered spatially so that any variable $\phi(x) = [\rho, \rho u, \rho v, \rho w, \rho E, \rho Y_w]$ is decomposed into a resolved part $\bar{\phi}(x)$ and a non-resolved (or sub-grid scale) part $\phi''(x)$, with $\phi(x) = \bar{\phi}(x) + \phi''(x)$. For compressible flows, Favre-filtered variables are used, defined as $\bar{\phi}(x) = \bar{\phi}(x) + \phi''(x)$, with $\bar{\phi} = \bar{\rho}\bar{\phi}/\bar{\rho}$. Using this approach, dimensionless Favre-averaged Navier-Stokes equations are (Paoli & al. (2003)):

$$\frac{\partial \bar{\rho}}{\partial t} + \frac{\partial (\bar{\rho} \tilde{u}_j)}{\partial x_j} = \omega, \quad (2.1)$$

$$\frac{\partial (\bar{\rho} \tilde{u}_i)}{\partial t} + \frac{\partial (\bar{\rho} \tilde{u}_i \tilde{u}_j)}{\partial x_j} + \frac{\partial \bar{p}}{\partial x_i} = \frac{1}{Re} \frac{\partial \tilde{\tau}_{ij}}{\partial x_j} + \frac{\partial \sigma_{ij}}{\partial x_j}, \quad (2.2)$$

$$\frac{\partial (\bar{\rho} \tilde{E})}{\partial t} + \frac{\partial [(\bar{\rho} \tilde{E} + \bar{p}) \tilde{u}_j]}{\partial x_j} = \frac{1}{Re} \frac{\partial \tilde{\tau}_{ij} \tilde{u}_i}{\partial x_j} + \frac{\partial \sigma_{ij} \tilde{u}_i}{\partial x_j} - \frac{1}{Re Pr} C_p \frac{\partial \tilde{q}_j}{\partial x_j} - \frac{\partial Q_j}{\partial x_j}, \quad (2.3)$$

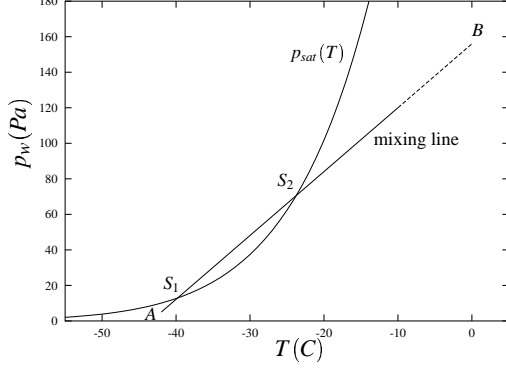


FIGURE 1. Thermodynamic conditions for ice formation: $p_s(T)$ is the saturation curve with respect to ice. States A and B represent, respectively, cold atmospheric and hot exhaust conditions (the distance between A and B is exaggerated). States S_1 and S_2 define the range of supersaturation, $p_w > p_{sat}(T)$.

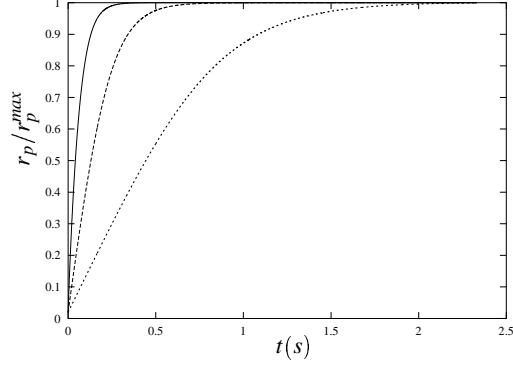


FIGURE 2. Theoretical evolutions of particles radius for different initial Knudsen numbers, $Kn(0) = \lambda/r_p(0)$ where λ is the mean free path of vapor molecule and $r_p(0) = 0.02 \mu m$ is the dry soot particle: —, $Kn(0) = 2.5$; ---, $Kn(0) = 10$; ·····, $Kn(0) = 36$.

$$\frac{\partial(\bar{\rho}\tilde{Y}_w)}{\partial t} + \frac{\partial(\bar{\rho}\tilde{Y}_w\tilde{u}_j)}{\partial x_j} = \frac{1}{ReSc} \frac{\partial}{\partial x_j} \left(\mu \frac{\partial \tilde{Y}_w}{\partial x_j} \right) + \frac{\partial \xi_j}{\partial x_j} + \omega. \quad (2.4)$$

The source term ω is due to ice nucleation and is responsible for vapor/ice mass coupling in the continuity and scalar equations, as detailed in the next Sections. The sub-grid scale (SGS) stress tensor $\sigma_{ij} = -(\bar{\rho}\tilde{u}_i\tilde{u}_j - \bar{\rho}\tilde{u}_i\tilde{u}_j)$, the SGS heat flux $Q_j = \bar{\rho}C_p\tilde{T}u_j - \bar{\rho}C_p\tilde{T}\tilde{u}_j$ and the SGS scalar flux $\xi_j = -(\bar{\rho}\tilde{Y}_w u_j - \bar{\rho}\tilde{Y}_w\tilde{u}_j)$ are modeled through sub-grid-scale eddy-viscosity concept:

$$\sigma_{ij} - \frac{1}{3}\sigma_{kk}\delta_{ij} = -2\mu_{sgs} \left(\tilde{S}_{ij} - \frac{1}{3}\delta_{ij}\tilde{S}_{kk} \right), \quad Q_j = -\frac{\mu_{sgs}C_p}{Pr_t} \frac{\partial \Theta}{\partial x_j}, \quad \xi_j = -\frac{\mu_{sgs}}{Sc_t} \frac{\partial \tilde{Y}_w}{\partial x_j} \quad (2.5)$$

where $\Theta = \tilde{T} - \frac{1}{2\bar{\rho}C_p}\sigma_{kk}$ is the modified temperature while turbulent Prandtl and Schmidt numbers are assumed to be constant, $Pr_t = 0.3$ and $Sc_t = 0.3$ (these are good approximations for shear flows, according to dynamic model LES by Moin & al. (1991)). Sub-grid scale viscosity μ_{sgs} is obtained through the Filtered Structure Function model (Ducros & al. (1996)), initially developed in spectral space and then transposed into physical space. This model was found to be well suited for the simulation of transitional flows because it induces no SGS viscosity when there is no energy at the cutoff wavelength (Ducros & al. (1996), Le Dizès & Laporte (2002)).

2.1. Particles treatment

The Lagrangian particle tracking approach has been adapted to the present problem of ice formation. On one hand, due to their small size (the radius r_p varying from tens of nanometers to a few microns, during the early contrail evolution, see Karcher & al. (1996)), the particles relaxation time $\tau_p = 4\rho_p r_p^2 / 18\mu$ remains short ($10^{-8}s$ to $10^{-5}s$) and negligible compared to the characteristic times at the filtered size. This allows to treat them as tracers which follow the carrier phase. On the other hand, strong mass exchanges between the ice and vapor phases takes place because of the large particles number density, varying between 10^9 and $10^{11} m^{-3}$, a few seconds after the emission (Karcher & al. (1996)). This also implies that only packets of particles, or "numerical particles", can be carried, each one containing a large number n_{trans} of real soot-ice kernels (as discussed in Paoli & al. (2002), this approach can be seen as a particular case of the method of moments used to solve a Liouville equation for particles conservation in four-dimensional space (x, y, z, r_p)). A numerical particle can be thought as the center of mass, \underline{x}_p , of n_{trans} physical

particles. In the tracer limit, its motion is completely described by:

$$\frac{d\mathbf{x}_p}{dt} = \tilde{\mathbf{u}}(\mathbf{x}_p) \quad (2.6)$$

where $\tilde{\mathbf{u}}$ is the (filtered) gas velocity at \mathbf{x}_p . Using filtered quantities in (2.6) is equivalent to neglect sub-grid dispersion, compared to the resolved, large scale dispersion (due to the high Reynolds number).

Gas sources are estimated at the numerical particle positions with point force approximation (see Boivin & *al.* (1998), Yeung & Pope (1988)). Afterwards they are projected on the Eulerian grid, that is equivalent to the application of a spatial filtering (Boivin & *al.* (1998)). Although complete exchange between phases (full two-way coupling) is allowed (H  lie & *al.* (2002)), drag momentum exchange remains negligible due to the tracer limit and the solid/gas mass ratio. Temperature cannot be modified by ice growth by more than a few Kelvin (Schumann (1996)), so that thermal exchanges from particles to gas are also neglected. Hence, only mass exchange is considered, i.e. vapor condensation over soot particles through the source term ω .

2.2. Ice-growth model

The term $\omega = \dot{\rho}_w$ is found to be negligible in (2.1) because of the small amount (order of few percent) of water vapor in the exhaust gases. On the other hand, in (2.4), it accounts for vapor/ice phases exchange and is related to the radius growth, \dot{r}_p , of a single ice crystal \dot{r}_p , by a simple, diffusional law by Karcher & *al.* (1996). In dimensionless form, \dot{r}_p and $\dot{\rho}_w$ are given by (n_p is the total number of numerical particles and all bars and tildes are removed for simplicity):

$$\dot{r}_p = \frac{G(r_p)(Y_w - Y_{sat})}{\rho_p r_p Re Sc} \quad (2.7)$$

$$\dot{\rho}_w(\mathbf{x}) = - \sum_{p=1}^{n_p} n_{trans} \delta(\mathbf{x} - \mathbf{x}_p) 4\pi r_p^2 \rho_p \dot{r}_p \quad (2.8)$$

where ρ_p is the ice density and Y_{sat} is the vapor mass fraction at saturation (related to the molar fraction, X_{sat} , by $Y_{sat} = X_{sat} / (X_{sat} + (1 - X_{sat}) W_{air} / W_w)$, with $W_{air} = 28.85 \text{ Kg/Kmole}$, $W_w = 18.01 \text{ Kg/Kmole}$). Saturation conditions are estimated by Sonntag (1994)

$$p_{sat} = p X_{sat} = \exp(-6024.5282/T + 29.32707 + 1.0613868 \cdot 10^{-2} T - 1.3198825 \cdot 10^{-5} T^2 - 0.49382577 \ln T). \quad (2.9)$$

The collisional factor $G(r_p)$ in 2.7 is given by a semi-theoretical correlation, $G(r_p) = (1/(1 + Kn) + 40Kn/3)^{-1}$, which accounts for the transition from gas kinetic to the continuum regime (see Karcher & *al.* (1996)) and was found to give good results for quasi-isothermal flows and low heat transfer problems (Qu & Davis (2001)). It is parametrized by the Knudsen number, defined as the ratio of the vapor mean free path to the soot-ice kernel radius, $Kn = \lambda/r_p$. The mean free path is estimated through $\lambda = (\sqrt{2} \pi d^2 n)^{-1}$ which depends on the vapor molecular cross section πd^2 and the total number density n . Despite its simplicity, this model contains much of the essential physics of condensation by vapor diffusion, more sophisticated microphysics models can be found in atmospheric science literature (see Pruppacher & Klett (1997)).

A (zero-dimensional) system of equations 2.7 and 2.8 in r_p and Y_w can be integrated for given initial conditions $r_p(0)$ and $Y_w(0)$, if the total number of ice-soot kernels $N_p = n_p \times n_{trans}$, T and λ are assigned. Typical values for the engine exhausts at flight conditions are $T = 220 \text{ K}$ and $Y_w(0) = 0.03$ (Garnier & *al.* (1997)), while the evaluation of the initial soot particles size and distribution is more difficult and can widely vary according to the engines. Following Karcher & *al.* (1996), a reasonable choice is $r_p(0) = 0.02 \mu\text{m}$ and $N_p = 2.5 \times 10^{11}$ (obtained by a soot number density of $0.9 \times 10^{11} \text{ m}^{-3}$ and a volume $1 \times \pi r_{jet}^2$, with $r_{jet} = 1 \text{ m}$). Moreover, due to

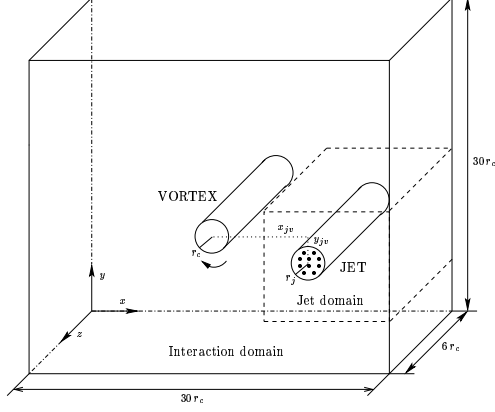


FIGURE 3. Sketch of the computational domains for the jet and the interaction phases.

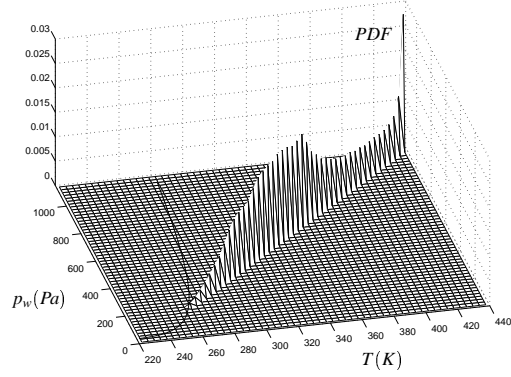


FIGURE 4. Joint PDF of temperature and water vapor partial pressure around passive particles at $t = 0.6 s$ (the saturation curve p_{sat} is also shown).

uncertainties in the evaluation of the exact cross-section of water vapor molecule, three values of λ have been considered to check the sensitivity of the ice growth process. Figure 2 shows that reducing λ increases the growth rate whereas it does not affect the final value of the radius which corresponds to the thermodynamic equilibrium state at the (fixed) saturation conditions.

2.3. Numerical scheme

The numerical code is a three-dimensional finite differences solver. For the gas phase, space discretization is performed by a sixth-order compact scheme (Lele (1992)). Time integration is performed by means of a three-stage Runge-Kutta method, for both phases. The projection of source terms at the particle position (x_p, y_p, z_p) on the eight closest fixed grid points x_i, y_i, z_i is made inversely to the volume $|(x_p - x_i)(y_p - y_i)(z_p - z_i)|$ (Boivin & al. (1998)), through a liner interpolation scheme to take advantage of its bounding properties. Boundary conditions are periodic in the z -direction, and non-reflective outlet in the others, using the NSCBC technique (Poinsot & Lele (1992)). The solver NTMIX3D is fully parallel, using domain decomposition.

3. Model problem and results

This section describes the results of the simulation of ice formation in the near-field of an aircraft wake. A two-stage simulation is used (Ferreira Gago & al. (2002), Paoli & al. (2003)): it consists in first simulating a temporal evolving jet ("jet phase") and, then, its interaction with the vortex ("interaction phase"). A sketch of the computational domain for the two phases is shown in Fig. 3. For the jet phase it has dimensions $L_x = L_y = 16 r_j$ and $L_z = 6 r_j$, z being the jet axis and $r_j = 1 m$ the exhaust jet radius, and consists of $161 \times 161 \times 61$ grid points; for the interaction phase, the dimensions are $L_x = L_y = 30 r_c$ and $L_z = 6 r_c$ with $301 \times 301 \times 61$ grid points, where $r_c = r_j$ is the vortex core. The jet Reynolds number and Mach number are, respectively, $Re = r_j w_j / \nu = 3.2 \cdot 10^6$ and $M = 0.2$. Axial velocity, temperature and vapor mass fraction are initialized according to a \tanh law:

$$\begin{aligned} w_0(r) &= \frac{1}{2} \left[(w_j + w_a) - (w_j - w_a) F(r) \right], & T_0(r) &= \frac{1}{2} \left[(T_j + T_a) - (T_j - T_a) F(r) \right], \\ Y_{w0}(r) &= \frac{1}{2} \left[(Y_{wj} + Y_{wa}) - (Y_{wj} - Y_{wa}) F(r) \right] & \text{with } F(r) &= \tanh \left[\frac{1}{4} \frac{r_j}{\theta} \left(\frac{r}{r_j} - \frac{r_j}{r} \right) \right] \end{aligned} \quad (3.1)$$

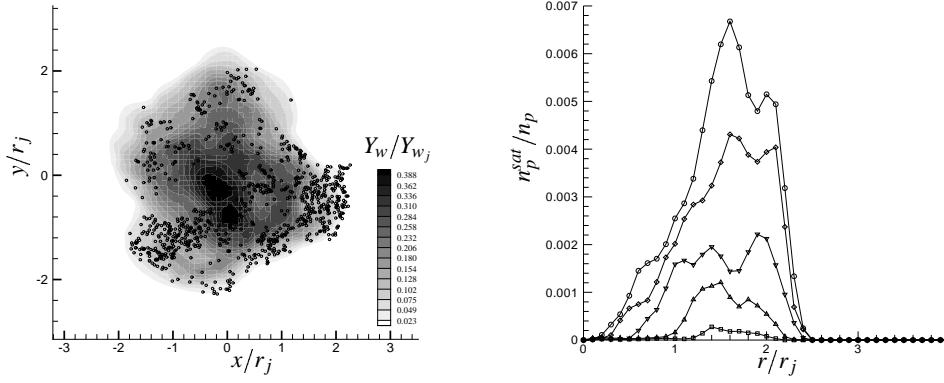


FIGURE 5. Jet phase: a) plane cut of vapor content and distribution of supersaturated particles ($t = 0.73\text{ s}$); b) evolution of the radial distribution of supersaturated particles: \square , $t = 0.6\text{ s}$; \triangle , $t = 0.63\text{ s}$; ∇ , $t = 0.67\text{ s}$; \diamond , $t = 0.7\text{ s}$; \circ , $t = 0.73\text{ s}$.

where r is the radial distance from the center; $r_j/\theta = 10$; while subscripts j and a indicate, respectively, exhaust jet and ambient air. In the present study no coflow is assumed, $w_a = 0$, and the background water content is zero, $Y_{w_a} = 0$. The exhaust water content, taken from available literature data (Garnier & al. (1997)), is $Y_{w_j} = 0.03$, while ambient and exhaust temperatures are, respectively, $T_a = 220\text{ K}$ and 440 K , giving $T_j/T_a = 2$. The jet is loaded with $n_p = 250000$ (numerical) soot particles with the same radius $r_p(0) = 0.02\text{ }\mu\text{m}$. They behave as tracers (see (2.6)) and each one represents a packet of $n_{trans} = 10^6$ physical particles. A random noise perturbation δw is added to the base flow velocity w_0 in (3.1) to trigger jet instability and transition to turbulence. When the maximum jet velocity has decreased to half its initial value (see Ferreira Gago & al. (2002), Paoli & al. (2003) for details), the second stage of the computation begins: the domain is enlarged and a vortex inserted ($x_{jv} = 5r_c$ and $y_{jv} = -r_c$, see Fig. 3), according to the Lamb-Oseen model: $v_\theta(r) = \alpha v_c r_c/r [1 - \exp(-\beta(r/r_c)^2)]$ where $\alpha = 1.4$, $\beta = 1.2544$ and $v_c = 1/1.5 w_j$ is the vortex core velocity.

3.1. Passive tracers results

A first set of LES was performed with passive particles and the ice-growth model switched off, $\omega = 0$. This provided a reference mixing case for typical aircraft wake configurations, where different initial conditions could be used with the same simulation. It was also useful to analyze the spatial distribution of supersaturated particles and identify the regions where ice formation is most likely to occur. Basic diagnostic consists in analyzing the thermodynamic properties of the exhaust gas during mixing with ambient air. Probability Density Function (PDF) is used to identify the particles that upersaturate with respect to ice. Figure 4 shows the joint PDF of normalized temperature, $(T - T_a)/(T_j - T_a)$, and water vapor partial pressure, $(p_w - p_{w_a})/(p_{w_j} - p_{w_a})$, around soot particles. The PDF follows a straight line which indicates pure mixing between hot jet and cold air. This is a consequence of low Mach number and $Le = Sc/Pr = 1$ assumption. The first one implies small pressure fluctuations and kinetic energy negligible compared to internal energy in (2.3). The latter implies the same diffusion terms in (2.3) and (2.4). Therefore, T and p_w are solved by the same transport equations and evolve along a mixing line

$$\frac{p_w}{p_{w_j} - p_{w_a}} = \frac{T}{T_j - T_a} + \frac{1}{2} \left(\frac{p_{w_j} + p_{w_a}}{p_{w_j} - p_{w_a}} - \frac{T_j + T_a}{T_j - T_a} \right). \quad (3.2)$$

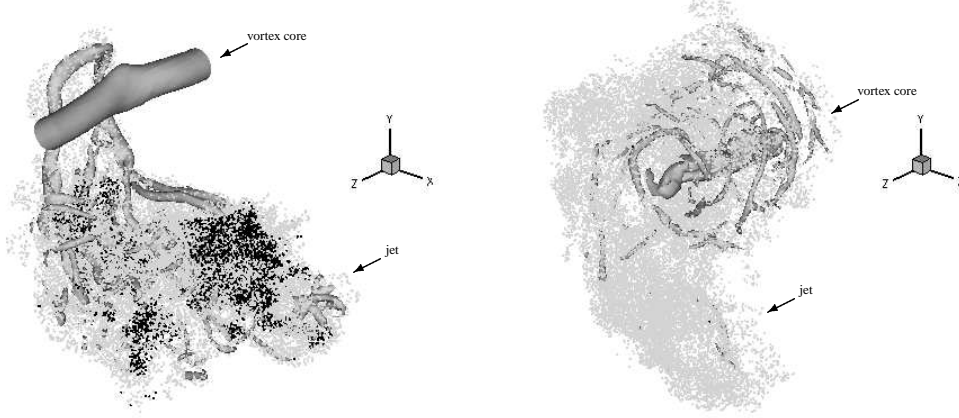


FIGURE 6. Passive particles distribution during the jet/vortex interaction phase: left, $t = 1$ s; right, $t = 1.7$ s. Dry soot particles are represented in black, iced supersaturated particles in white grey. The iso-surface of the vorticity magnitude (in dark grey) identifies the vortex and the secondary structures around the core.

(obtained by elimination of r in (3.1)). All particles are initially placed below the saturation curve p_{sat} because they are still concentrated inside the hot jet region. Due to the mixing with cold air, particles cool, down moving along the mixing line, until some of them become supersaturated (crossing of p_{sat} curve at $t = 0.6$ s). The spatial distribution of supersaturated particles is provided in Fig. 5 (left) together with a plane cut of water vapor content during the jet phase. The figure shows that air first saturates around the particles at the edges of the jet where temperature has dropped and there is sufficient vapor to condense. This is quantified in Fig. 5 (right) which shows the number of supersaturated particles as a function of the radial distance from the jet. The large peak at $r = 1.5 r_j$ identifies the region of maximum accumulation of saturated nucleation sites. The dynamics during the interaction phase is dominated by the entrainment of the exhaust jet by the wake vortex (see Fig. 6). When the jet is close enough to the vortex core, its axial velocity strongly interacts with the vortex tangential velocity, causing the formation of three-dimensional structures of azimuthal vorticity. These structures progressively decay corresponding to complete entrainment of the jet (Paoli & *al.* (2003)). This mechanism of entrainment enhances mixing with external air. Exhaust cooling and vapor condensation are favored by the presence of the vortex, as indicated in Figure 6 (right) which shows that all particles are supersaturated at $t = 1.7$ s, thus indicating that the contrail can form everywhere in the wake.

3.2. Freezing particles results

This section presents the results of the simulations by activating the ice-growth model, (2.7) and (2.8), with an initial Knudsen $Kn(0) = 2.5$. The goal is to analyze how the contrail forms, grows and influences vapor mixing. Figure 7 displays the temporal evolution of the mean crystal radius, $r_p^{mean} = \sqrt{\sum_p r_p^2 / n_p}$. Up to $t \simeq 0.7$ s, corresponding to the end of the jet phase, r_p^{mean} slightly changes with respect to the initial dry particle size, $r_p(0) = 0.02 \mu m$. It starts to grow at the beginning of the interaction phase when the high supersaturation $Y_w - Y_{sat}$ induced by the jet turbulent diffusion and the presence of the vortex significantly increases the growth rate dr_p/dt . Later on, at $t \simeq 2$ s the growth slows down and finally the mean crystals radius reaches a plateau value of $r_p^{mean} \simeq 4.25 \mu m$ at $t = 3$ s. This is explained by observing that, as long as particles freeze, exhaust vapor is either removed or diluted in the jet plume by large-scale vortex entrainment and turbulent diffusion (Paoli & *al.* (2003)). This reduces the mass fraction Y_w , the local supersaturation and the growth rate dr_p/dt , as indicated by 2.7. Associated to the growth of particles radius, the total mass of ice $m_{ice} = \sum_p 4/3 \pi \rho_p r_p^3$ increases, reaching the remarkable value of 60% of the

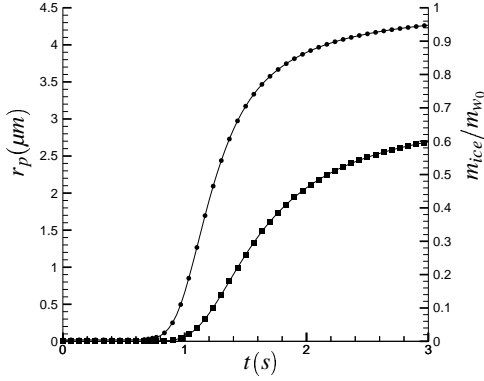


FIGURE 7. Evolutions of particles mean radius, r_p^{mean} (—●—), and total ice mass normalized by the initial water vapor content, m_{ice}/m_{w0} (—■—).

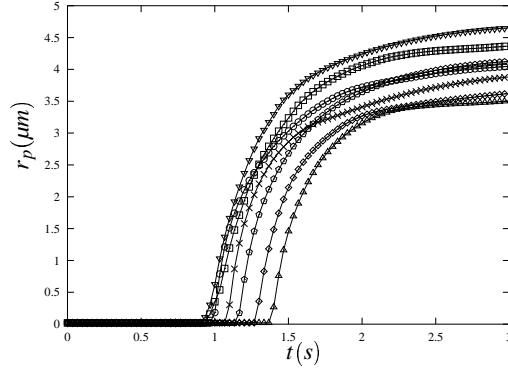


FIGURE 8. Time history of sample particles radius, showing that particles freezing first grow faster.

total initial vapor mass content. A general feature of the interaction is that particles which freeze first attain the larger asymptotic radius, as shown in Fig. 8, because they find more vapor available for condensation. In particular, after complete entrainment by the vortex, larger ice crystals are equi-distributed as a function of the distance from the center (not shown). The strong mass exchange by vapor removal affects exhaust dilution properties: in fact, vapor partial pressure p_w decreases at a faster rate than temperature T (the latent heat of condensation is negligible, Schumann (1996)) which causes a significant deviation from the theoretical mixing line, as shown in Fig. 9 (left). The figure reports the scatter plot of p_w and T interpolated around each particle at different times during the interaction phase. It also shows that particles enter the supersaturation region in the thermodynamic plane (T, p_w) , then move towards and finally collapse onto the saturation curve p_{sat} . This indicates that thermodynamic equilibrium between vapor and ice phases is reached according to the local thermodynamic conditions experienced by each particle. For the sake of completeness, Fig. 9 (right) reports the same scatter plot for a case where (only) the jet is run up to the same final time and with the same initial conditions. As the dilution of the exhaust into cold air is not enhanced by the vortex entrainment, particles are closer to the mixing line and supersaturation $S = p - p_{sat}$ is higher (note that, from (2.7), $dr_p^2/dt \approx S$, leading to $r_p^{mean} \simeq 4.5 \mu m$ instead of $4.25 \mu m$). On the other hand, the extent of the supersaturation region in the wake is smaller because the exhaust plume area is smaller, as discussed in detail by Paoli & al. (2003), see also Fig. 6.

The distribution of ice crystals size is provided in Fig. 10 in terms of radius PDF. The peak around $r_p(0) = 0.02 \mu m$ at $t = 0.73$ s (end of the jet phase) indicates that only a small amount of ice has formed. As long as ice nucleation proceeds, such a peak decreases and finally disappears, and the shape of the PDF finally approaches a Gaussian at $t = 3$ s. An important result for contrail optical properties is the variance, $var(r_p)/r_p^{mean} \simeq 0.125$, which indicates polydispersion whereas temperature and partial pressure around particles has become approximatively uniform. Figure 11 finally presents the normalized PDF of water vapor mass fraction Y_w in the overall domain, which identifies the instantaneous state of the available water vapor. Initially the PDF is characterized by a quasi two-delta function at 0 and $Y_w = 0.03$ (not shown). The figure reports the PDF at $t = 1.7$ s, which corresponds to the highest mass exchange between the two phases. Three cases are presented. The first one corresponds to the passive particles, with a typical beta-like shape and non negligible PDF for relatively large values of vapor $Y_w > 1.5 \cdot 10^{-3}$. The second corresponds to the active model results in the case of a slow growing process (large initial Knud-

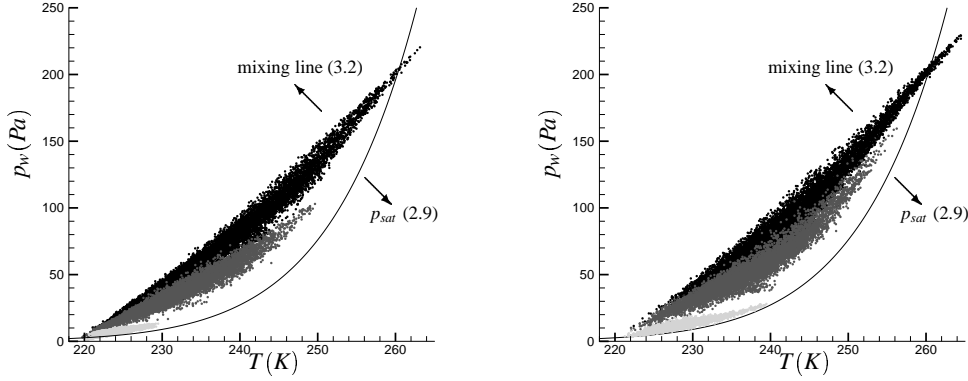


FIGURE 9. Scatter plot of temperature T and vapor partial pressure p_w around particles at different times from the emission (black scats, $t = 1.4$ s; dark grey, $t = 1.7$ s; white grey, $t = 3$ s): left, jet and wake vortex; right, jet alone.

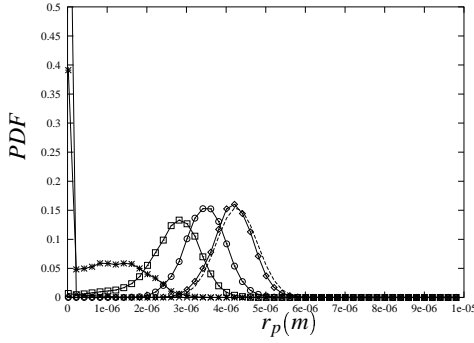


FIGURE 10. PDF of particles radius during the interaction phase: \times —, $t = 0.7$ s; $*$ —, $t = 1$ s; \square —, $t = 1.4$ s; \circ —, $t = 1.7$ s, \diamond —, $t = 3$ s; — — —, $t = 3$ s (Gaussian).

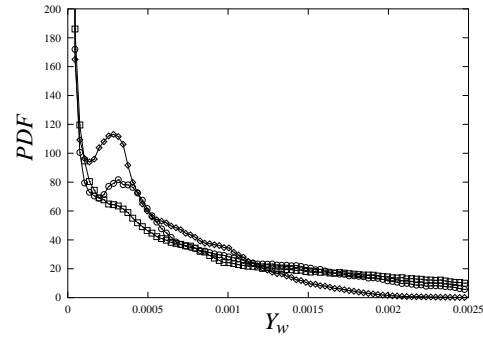


FIGURE 11. PDF of water vapor field over the entire domain at $t = 1.7$ s: \square —, passive tracers; \circ —, $Kn(0) = 36$; \diamond —, $Kn(0) = 2.5$.

sen number), and the third curve corresponds to a fast growing process (low initial Knudsen number). The figure shows the occurrence of a large transport of vapor mass by phase exchange from $Y_w > 1.5 \cdot 10^{-3}$ to the lower values around $Y_w \simeq 3 \cdot 10^{-4}$, as confirmed by the appearance of a peak in the PDF (weaker in the case of higher Knudsen because of the slower ice growth). Figure 11 demonstrates that the freezing of vapor surrounding the large ice particles, illustrated in Figs. 7 and 9, directly affects the vapor content which is still available for the other particles. This full-coupling process explains the radii polydispersion.

4. Conclusions and perspectives

The formation and early evolution of a contrail in the near-field of an aircraft wake was studied by using a mixed Eulerian/Lagrangian two-phase flow model, coupled to a simple microphysics model for condensation. The simulations were carried out with and without the model activated the main objectives being: first, to characterize the contrail tridimensional structure, as the distribution of supersaturation in the wake; then, to understand whether and how, accounting for tridimensional exhausts dispersion in the wake and for vapor depletion by condensation, affect zero-dimensional theories on contrail formation. For example, it was shown that the classical

"mixing" assumption used to predict ice formation may not be verified when a full coupling between ice and vapor phases is used. An interesting extension to this work would be to analyze the interaction between an exhaust jet and a vorticity sheet to find out how its turbulence further modify exhausts dispersion and ice growth. Finally, the proposed formulation for contrail LES could be suitably improved and "enriched" in the future by the expected progresses in the understanding of ice microphysics and/or its interaction with atmospheric turbulence.

The authors wish to thank the CINES for providing computational resources and COS (Comit   d'Orientation sur le Supersonique) for support. The simulations were initiated at the 2002 Summer Program of the Center for Turbulence Research which is gratefully acknowledged.

REFERENCES

- BOIVIN, M., SIMONIN O. & SQUIRES K. D. 1998 Direct numerical simulations of turbulence modulation by particles in isotropic turbulence. *J. Fluid Mech.* **375**, 235-263.
- DUCROS F., COMTE P. & LESIEUR M. 1996 Large-Eddy Simulation of transition to turbulence in a boundary layer spatially developing over a flat plate. *J. Fluid. Mech.*, **326**, 1-36.
- GARNIER, F., BAUDOIN, C., WOODS P., & LOUISNARD, N. 1997 Engine emission alteration in the nearfield of an aircraft. *Atmos. Environ.* **31**, 1767-1781.
- FERREIRA GAGO, C., BRUNET, S., & GARNIER F. 2002 Numerical Investigation of turbulent mixing in a jet/wake vortex interaction. *AIAA J.* **40**, 276-284.
- GIERENS, K. M. 1996 Numerical simulations of persistent contrails. *J. Atmos. Sci.* **53**, 3333-3348.
- H  LIE, J., BEDAT, B., SIMONIN, O. & POINSOT, T. J. 2002 Analysis of mixture fraction fluctuations generated by spray vaporisation. *Proc. ICNC Conference*, SIAM, Sorrento (Italy).
- INTERGOVERNMENTAL PANEL OF CLIMATE CHANGE 1999 *Aviation and the Global Atmosphere*. Cambridge Univ. Press.
- KARCHER, B., PETER, T., BIERMANN, U. & SCHUMANN, U. 1996 The initial composition of jet condensation trails. *J. Atmos. Sci.* **53**, 3066-3083.
- LE DIZ  S, S. & LAPORTE, F. 2002 Theoretical predictions for the Elliptic instability in a two-vortex flow. *J. Fluid Mech.* **471**, 169-201.
- LELE, S. K. 1992 Compact finite difference scheme with spectral-like resolution. *J. Comp. Phys.* **103**, 16-42.
- MOIN, P., SQUIRES, K., CABOT, W., LEE, S. 1991 A dynamic subgrid-scale model for compressible turbulence and scalar transport. *Phys. Fluids* **11**, 2746-2757.
- PAOLI, R., H  LIE, J., POINSOT, T., & GHOSAL, S. 2002 Contrails formation in aircraft wakes using large-eddy simulations., *Proc. Summer Program of the Center for Turbulence Research*, Stanford, 229-241.
- PAOLI, R., LAPORTE, F., CUENOT, B., & POINSOT, T. 2003 Dynamics and mixing in jet/vortex interactions. *Phys. Fluids* **15**, 1843-1860.
- POINSOT, T. & LELE, S. K. 1992 Boundary Conditions for Direct Simulations of Compressible Viscous Flows. *J. Comp. Phys.* **101**, 104-129.
- PRUPPACHER, H. R. & KLETT J. D. 1997 *Microphysics of Clouds and Precipitation*. Kluwer, Dordrecht, The Netherlands.
- QU, X. & DAVIS E. J. 2001 Droplet evaporation and condensation in the near-continuum regime. *J. Aerosol Sc.* **32**, 861-875.
- SCHUMANN, U. 1996 On the conditions for contrail formation from aircraft exhausts. *Meteorol. Z.* **5**, 4-23.
- SONNTAG, D. 1994 Advancements in the field of hygrometry. *Meteorol. Z.* **3**, 51-66.
- SUSSMANN, R. & K. GIERENS 1999 Lidar and numerical studies of the different evolution of vortex pair and secondary wake in young contrails. *J. Geophys. Res.* **104**, 2131-2142.
- TRAVIS, D. J., CARLETON A. M. & LAURITSEN R. G. 2002 Contrails reduce daily temperature range. *Nature* **418**, 601.
- YEUNG, P.K. & POPE, S.B. 1988 An algorithm for tracking fluid particles in numerical simulations of homogeneous turbulence. *J. Comp. Phys.* **79**, 373-416.